The two-dimensional flow of a foam through a constriction: Insights from the bubble model

Vincent J. Langlois

Articles you may be interested in

Bubble migration in two-dimensional foam sheared in a wide-gap Couette device: Effects of non-Newtonian rheology
J. Rheol. **58**, 1809 (2014); 10.1122/1.4892660

On the effectiveness of a quasistatic bubble-scale simulation in predicting the constriction flow of a two-dimensional foam
J. Rheol. **56**, 457 (2012); 10.1122/1.3687301

Modeling and simulation of multiple bubble entrainment and interactions with two dimensional vortical flows
Phys. Fluids **23**, 023301 (2011); 10.1063/1.3541813

Local description of the two-dimensional flow of foam through a contraction
J. Rheol. **54**, 741 (2010); 10.1122/1.3380852

Dynamics of a two-dimensional upflowing mixing layer seeded with bubbles: Bubble dispersion and effect of two-way coupling
Phys. Fluids **18**, 103304 (2006); 10.1063/1.2363968

The two-dimensional flow of a foam through a constriction: Insights from the bubble model

Vincent J. Langlois[a]

Laboratoire de Géologie de Lyon, Université Claude Bernard Lyon 1/ENS de Lyon/CNRS, 2 rue Raphaël Dubois, 69100 Villeurbanne, France

Synopsis

The flow of a two-dimensional foam through a constriction is investigated numerically with the bubble model, and results are compared with existing experimental and numerical studies. We predict the dynamical behavior of the foam by measuring its flowrate as a function of the imposed pressure drop. We show that two flow regimes can be observed, with an affine relationship between flowrate and pressure drop. The model also shows that the flowrate increases with the width of the distribution of bubble sizes. The simulations exhibit a power law dependency of the flowrate in the width of the constriction. The local properties of the flow are also investigated by measuring the velocity field, the frequency and direction of plastic events, and main orientations of strain. We show that the main qualitative features of the plastic and strain tensors fit with existing experiments. Finally, we test a theoretical model that predicts a relationship among plasticity, deformation, and strain. © *2014 The Society of Rheology*. [http://dx.doi.org/10.1122/1.4872058]

I. INTRODUCTION

Liquid foams are complex fluids that can exhibit elastic, plastic, and viscous behaviors when flowing [Weaire and Hutzler (1999); Höhler and Cohen-Addad (2005)]. In the past decade, the characterization of their rheology has been the subject of many experimental and numerical studies. For practical reasons, many of them have focused on different kinds of two-dimensional (2D) foams (free bubble raft, bubble raft confined under a glass plate, or bubbles in a Hele-Shaw cell). In particular, the presence of a yield stress, the shear-thinning properties, or the development of shearbands have been widely investigated [Debrégeas *et al.* (2001); Lauridsen *et al.* (2004); Denkov *et al.* (2005); Katgert *et al.* (2008); Langlois *et al.* (2008)]. Continuous models able to account for the various properties observed in experiments and simulations have been proposed, using a viscoelastoplastic rheological description [Janiaud *et al.* (2006); Marmottant *et al.* (2008); Saramito (2009)]. More recently, the nonlocal rheological effects evidenced in emulsions by Goyon *et al.* (2008) and modeled by Bocquet *et al.* (2009) have been included in continuous models applied in the context of foams by Katgert and van Hecke (2010) and Barry *et al.* (2011). However, if the behavior of a foam in a Couette rheometer or under

---

[a]Electronic mail: vincent.langlois@univ-lyon1.fr

simple shear is now well understood, theoretical predictions have to be confirmed in more complex geometries.

Two geometries have been widely used in rheological experiments on various complex fluids such as emulsions, polymer solutions, or gels: The flow around an obstacle and the flow through a constriction, where the fluid experiences a brutal contraction followed by an expansion (that is, both shear and extensional strain). The former case was studied experimentally with 2D foams by Dollet *et al.* (2005b) and Dollet and Graner (2007), and the predictions of a continuous viscoelastoplastic model in such a geometry have been successfully tested [Cheddadi *et al.* (2011)]. The geometry of a constriction was also recently chosen as a benchmark to investigate various models of 2D liquid foams [Dollet (2010); Jones *et al.* (2011); Jones and Cox (2012)]: Experimental observations have been compared with predictions of simulations based on energy minimization {Surface Evolver[1] and Potts model [Jiang *et al.* (1999)]}.

The aim of this paper is to apply the bubble model to the same type of flow. This model was initially introduced in the context of 2D foam rheology in 1995 by Durian (1995, 1997) and consists in describing a foam as an assembly of soft disk-shaped or spherical bubbles rather than as a network of elastic films or vertices. It was later shown by Langlois *et al.* (2008) that despite its simplicity, an extension of the bubble model was successful in reproducing the Herschel-Bulkley behavior of a foam under constant shear [Lauridsen *et al.* (2004); Denkov *et al.* (2005); Katgert *et al.* (2008)], as well as the presence of shearbands in such a flow when confining plates exert a viscous drag on the bubbles [Debrégeas *et al.* (2001); Weaire *et al.* (2008)]. More recently, Sexton *et al.* (2011) predicted a new flow regime in a simple shear flow at high strain rates: Bubbles get trapped in lanes despite their polydispersity, which results in a Bingham rheology. Tighe *et al.* (2010) proposed a generic model of the rheology of the bubble model, including the influence of the packing fraction. Using a model of the effect of lubrication forces in the thin film that separates two droplets in contact, Meeker *et al.* (2004) and Seth *et al.* (2011) developed a more realistic approach of the dynamics of a 3D emulsion. By taking into account hydrodynamic lubrication forces in the films, they introduce a coupling between the local repulsive and viscous forces which both become nonlinear and depend on the thickness of films (that is, on the local packing fraction). Interestingly, the rheological properties of this model are very similar to the outcomes of the bubble model (in which lubrication effects are not accounted for). Using the pair correlation function predicted by these simulations, Seth *et al.* (2011) then proposed an analytical derivation of the constitutive equation of the emulsion (Herschel-Bulkley of index $m = 0.50$). In all these studies based on the interaction of overlapping spheres, the behavior of the foam or emulsion has, however, always been restricted to the linear shear configuration (either between two walls or in Lees-Edwards boundary conditions) and not in nonhomogeneous flows.

Given the simplicity of its implementation in any geometry, the bubble model is a good candidate to test rheological benchmarks such as the flow through a constriction. It is a dynamic model and, therefore, is able to reproduce rapid flows. Besides, it applies more realistically to wet foams. It can then be seen as complementary to quasistatic models (such as those based on Surface Evolver, where mechanical equilibrium is achieved at each timestep) that describe more accurately dry foams and are less suitable to account for energy dissipation.

---

[1]Brakke, K., Surface Evolver, http://www.susqu.edu/facstaff/b/brakke/evolver/.

The article is organized as follows: In Sec. II, we describe the implementation of the bubble model; in Sec. III, we predict the relation between discharge and pressure drop across the constriction and demonstrate the role of polydispersity. Finally in Sec. IV, we study the local properties of the flow and compare them to experimental results.

II. NUMERICAL MODEL

The 2D foam, as described by the bubble model, consists in a monolayer of spherical bubbles (that we represent, seen from above, as disks). The flow of the foam is computed by solving Newton's equation of motion for each individual bubble, using classical numerical techniques originally developed for Molecular Dynamics [Pöschel and Schwager (2005)].

A. Description of the setup

1. Geometrical characteristics

Experimentally, two different techniques have been used to push a 2D foam through a constriction: Bertho *et al.* (2006) confined a layer of bubbles between a liquid bath and a tilted glass plate. Bubbles are driven upward by buoyancy all along the channel. Therefore, after the constriction, the liquid fraction becomes very high and bubbles do not constitute a foam anymore. In experiments by Dollet (2010) or Jones and Cox (2012), bubbles are confined between two horizontal glass plates. In order to push them through the constriction, the foam is first accumulated in a vertical chamber, which has the effect of imposing a given pressure drop between entrance and exit of the channel. The local pressure gradient, however, is not imposed as uniform.

Following the latter method, we study a numerical setup that consists of two parts (see Fig. 1): In the vertical section of height h, bubbles are accelerated by buoyancy. They are then pushed into the second section, which constitutes the channel itself: In this section, the confining plate is horizontal and contains a constriction in the y direction (see Fig. 2). Periodic boundary conditions are applied in the x-direction: Each bubble leaving the channel on the right side is reinjected on the left side, at the base of the vertical column. The channel has a width $W = 50\,R_0$ and a length $L = 120\,R_0$, where R_0 is the average bubble radius. In the whole article, except Sec. III B, the default setup includes, in the center
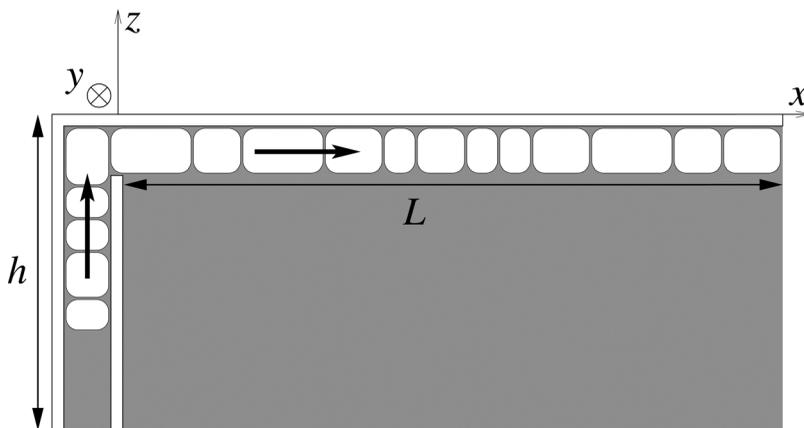

FIG. 1. Experimental device equivalent to the numerical setup, viewed from the side. Bubbles are accelerated by buoyancy over a height h before entering the horizontal channel of length L that contains the constriction.
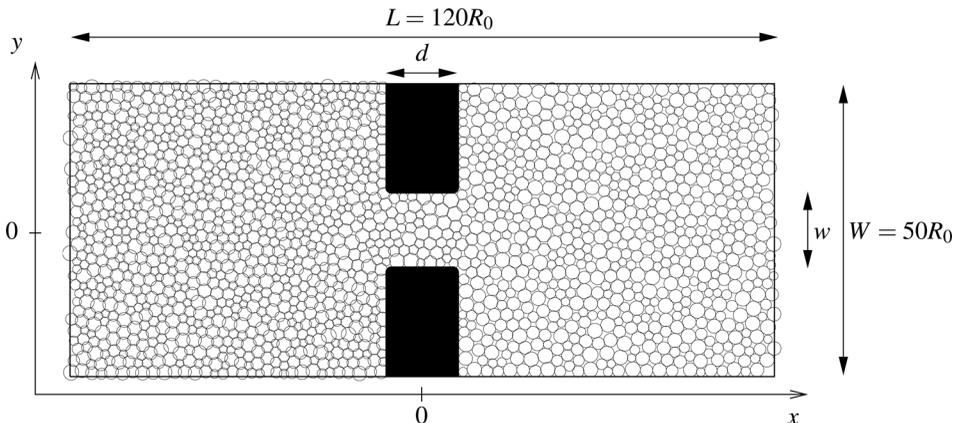
FIG. 2. Horizontal section of the setup, seen from above. Bubbles flow from left to right. The liquid fraction is visibly higher after the constriction than before (see Sec. IV A).

of the horizontal section, a constriction of width $w = W/4$ and length $d = w$. In order to avoid numerical singularities, the corners of the constriction are rounded with a radius of curvature equal to the mean bubble radius.

The essential difference between this numerical setup and experiments lies in the compressibility of the bubbles: In the bubble model, because of the overlaps, bubbles can be compressed, whereas in a Hele-Shaw cell (where the 2D foam is confined between two glass plates), bubbles can be considered as incompressible. However, an *apparent compressibility* in 2D can be observed if the foam sits below a glass plate but on top of a liquid bath [see Fig. 2 and Dollet *et al.* (2005a); Dollet and Graner (2007)]: In this configuration, bubbles are allowed to expand vertically, which can modify their apparent area (as viewed from above). Finally, let us note that in our simulation, the pressure drop is the control parameter and the flowrate is a result of the dynamics, whereas in most experimental devices [Dollet (2010); Jones and Cox (2012)], the flowrate is imposed.

2. Driving force

A buoyancy force applies to bubbles located in the vertical section

$$\mathbf{F}_d = \Delta\rho \, g \, V_b \, \mathbf{u}_z, \tag{1}$$

where V_b is the volume of the bubble, g is the gravitational acceleration, and $\Delta\rho$ is the density contrast between the liquid and gas phases. No external force is applied to bubbles once they enter the horizontal section. Because of the driving force, bubbles are pushed upward in the vertical channel, and consequently from left to right in the horizontal channel, toward the constriction: An effective pressure drop Δp appears between entrance and exit of the horizontal channel, with

$$\Delta p = \Delta\rho \, g \, h. \tag{2}$$

The effective pressure gradient applied between both ends of the channel is normalized by the typical elastic force on a bubble, per unit volume

$$\Gamma = \frac{\Delta p / L}{(\kappa R_0)/V_0} \, , \tag{3}$$

with $V_0 = (4\pi/3) R_0{}^3$ the volume of a bubble of mean radius R_0. κ is the constant of elasticity of bubbles [see Eq. (6)]. In order to keep the number of bubbles constant in all simulations, the height of the vertical channel is fixed at $h = 20 \, R_0$, and g is varied in order to impose increasing values of Γ.

3. Polydispersity and liquid fraction

The bubbles are initially randomly packed within the channel and column. The radius of each bubble is chosen within a uniform distribution of center R_0 and width ΔR. We characterize the polydispersity of the foam by the parameter

$$\delta = \Delta R / R_0. \tag{4}$$

In our study, the parameter δ varies between 0% and 22.5%. In a 2D foam, an apparent liquid fraction can be defined as the ratio between the apparent area of films and Plateau borders and the total area available to the foam. By analogy, one may define for the bubble model an effective 2D liquid fraction ϵ as

$$\epsilon = 1 - \frac{1}{W(L+h)} \sum_{i=1}^{N} \pi R_i{}^2, \tag{5}$$

where $W(L + h)$ is the total area where bubbles are packed, and N is the number of bubbles. Let us remark that in this definition, overlaps are neglected, and the parameter ϵ can, therefore, reach negative values. In the whole article, the *average* liquid fraction is chosen as $\epsilon = 0.1$, which corresponds to a relatively wet foam. We have not investigated the role of this parameter in the constriction flow. However, its influence on the rheology in simple shear flow was already independently studied by Tighe *et al.* (2010).

B. Interactions between bubbles

1. Repulsive force

Bubbles interact with one another through elastic and viscous forces, as in the original model developed by Durian (1997). Physically, two bubbles that are pushed into contact are distorted and their contact surface flattens out to form a film. The increase in total area generates a repulsive force between the two bubbles, that is, proportional to the liquid-gas surface tension. In the model, the exact deformation of two bubbles in contact is not accounted for: Both bubbles remain spherical, overlap, and experience a repulsive force. When overlapping (and only then), two bubbles /i/ and /j/ interact via a simple spring force. The displacement of the spring is equal to their radial overlap (see Fig. 3). The elastic repulsive force $\mathbf{F}_e$ that bubble j exerts on bubble i is given by

$$\mathbf{F}_e = \kappa \, \frac{2R_0}{R_i + R_j} \, \Delta_{ij} \, \mathbf{n}_{ij}, \tag{6}$$

where κ is the coefficient of elasticity, $\mathbf{n}_{ij}$ is the normal vector between bubbles i and j, defined by

$$\mathbf{n}_{ij} = \frac{\mathbf{r}_i - \mathbf{r}_j}{|\mathbf{r}_i - \mathbf{r}_j|}, \tag{7}$$

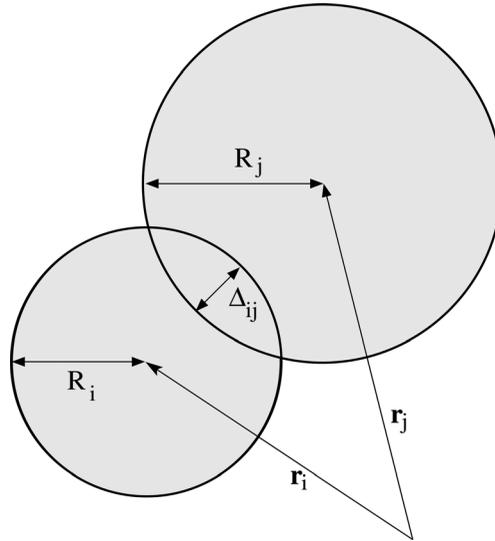and the overlap Δ_{ij} (see Fig. 3) is given by

FIG. 3. Overlap Δ_{ij} between two contacting bubbles of radii R_i and R_j, located at $\mathbf{r}_i$ and $\mathbf{r}_j$, respectively.

$$\Delta_{ij} = \begin{cases} (R_i + R_j) - |\mathbf{r}_i - \mathbf{r}_j| & \text{if } (R_i + R_j) < |\mathbf{r}_i - \mathbf{r}_j| \\ 0 & \text{otherwise,} \end{cases} \tag{8}$$

where R_i and R_j are the radii of bubbles i and j, centered at $\mathbf{r}_i$ and $\mathbf{r}_j$, respectively, and R_0 is the average bubble radius of the entire sample. The ratio $2R_0/(R_i + R_j)$ in Eq. (6) takes into account that larger bubbles are easier to deform than smaller ones (the Laplace pressure in each bubble being inversely proportional to its radius).

2. Dissipative force

A flowing foam dissipates energy by viscous friction in the films and Plateau borders separating the bubbles. Though the films are not explicitly represented in our model, we add a viscous component to bubble-bubble interactions. A realistic expression for such a force would be nonlinear in the relative velocity of the bubbles {the exponent itself depending on the surfactant properties [Bretherton (1961); Denkov *et al.* (2005)]}, and the viscous coefficient would depend on the viscosity of the liquid, the thickness of the contact film, and its exact shape [Meeker *et al.* (2004); Saugey *et al.* (2006)]. Contrary to the EHD model by Seth *et al.* (2011), lubrication forces are not accounted for in the bubble model, and the viscous force between two bubbles does not depend on the thickness of the film (that is, on the overlap Δ_{ij}). For sake of simplicity and in accordance with previous implementations of this model [Langlois *et al.* (2008); Sexton *et al.* (2011)], we simplify this interaction: The dissipative force $\mathbf{F}_v$ acting on a bubble i in contact with a bubble j reads

$$\mathbf{F}_v = -c_b(\mathbf{v}_i - \mathbf{v}_j), \tag{9}$$

where c_b is a dissipation constant and $\mathbf{v}_i$ and $\mathbf{v}_j$ are the respective bubble velocities. It has to be noted that despite the simplicity of the forces implemented in the bubble model, it exhibits the same rheological properties as the EHD model [Langlois *et al.* (2008)].

In particular, even if the local viscous force does not depend on the overlap, the resulting global rheology (and in particular the yield stress of the foam) nevertheless varies with the packing fraction [Tighe *et al.* (2010); Seth *et al.* (2011)].

C. Interactions with walls

1. Friction along the confining plate

The viscous friction along the glass plate is also modeled through a dissipative term, linear in both the bubble radius and velocity

$$\mathbf{F}_w = -c_w \frac{R_i}{R_0} \mathbf{v}_i. \tag{10}$$

The influence of the ratio between the two viscous coefficients c_w and c_b has already been investigated in the case of a simple shear flow [Langlois *et al.* (2008); Weaire *et al.* (2008)]. We choose here to restrain our study to the case $c_w = c_b$.

2. Interactions with channel walls

When a bubble comes in contact with one of the walls (either a lateral wall: $y = -W/2$ and $y = W/2$ or the constriction itself), it experiences a purely normal force, with a spring constant κ and a dissipative component c_b identical to a bubble-bubble collision. The tangential force is zero, making all walls frictionless {in experiments, sliding of bubbles is often observed at the walls if they are not specifically saw-toothed [Katgert *et al.* (2008); Dollet (2010)]}.

D. Time integration

At a given iteration, all forces acting on each bubble are computed. Overlaps between bubbles are found by using the linked cell algorithm [Pöschel and Schwager (2005)]. An effective mass is assigned to each bubble and we use the Verlet algorithm (of fourth order) [Pöschel and Schwager (2005)] to compute the position of each bubble at the next iteration from Newton's second law. The mass is chosen so that the motion of each bubble remains overdamped and inertia is, therefore, negligible in the dynamics: m_b being the mass of a bubble of radius R_0, the ratio $\kappa m_b/c_b^2$ is set to 1.5×10^{-2}. In order to compute accurately each collision between bubbles, the iterative timestep Δt is chosen as 100 times smaller than the characteristic viscous timescale

$$\Delta t = \frac{\tau_v}{100} \quad \text{with} \quad \tau_v = \frac{m_b}{c_b}. \tag{11}$$

For $N = 2000$ bubbles, the computation of $10^7 \times 10^6$ iterations takes the order of 2 days on a desktop PC.

III. FLOWRATE THROUGH THE CONSTRICTION

A. Hydraulic resistance

As in most experiments, the flowrate of bubbles $\tilde{Q}$ is defined as the total area of bubbles that cross the constriction ($x = 0$) per unit time. It is computed over 4×10^7 iterations once the stationary regime has been reached. It can be normalized in the following way:
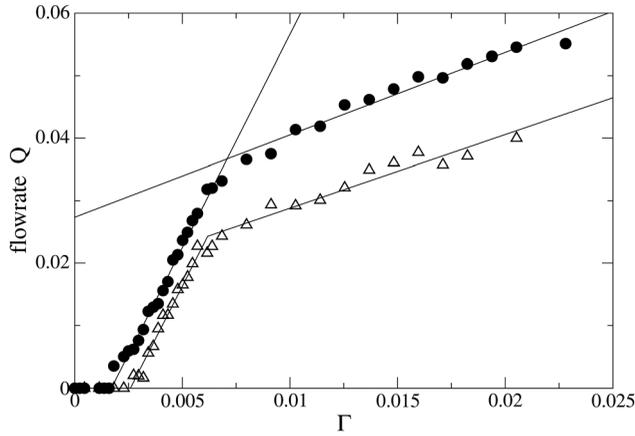
FIG. 4. Flowrate as a function of the pressure drop imposed to the foam for a polydispersity $\delta = 15\%$ (black disks) and $\delta = 2.5\%$ (empty triangles). Plain lines are best affine fits in their respective regions of validity.

$$Q = \frac{\tilde{Q}}{\pi R_0{}^2} \, \tau \, , \tag{12}$$

where $\tau = c_b/\kappa$ is the internal timescale of the material. This timescale characterizes the interplay between storage (through elastic forces) and dissipation of energy (through viscous forces). We have plotted the normalized flowrate as a function of Γ in Fig. 4 for a quasi-monodisperse ($\delta = 2.5\%$) and a strongly polydisperse ($\delta = 15\%$) foam. Below a given value Γ_0 of the pressure drop, there is no flow through the constriction, which is consistent with the existence of a yield stress. If this threshold is not reached, bubbles are pushed together before the constriction and energy is stored in their elastic deformation. Close to the threshold, the flow is intermittent: Bubbles form force chains and remain blocked for a certain amount of time before the chains break and a few bubbles pass the obstacle. Because this motion is very slow, the computation of Q can be dubious, which makes it difficult to assess directly the exact position of the threshold. Instead we can estimate its value by fitting the points measured in the flowing regime. As expected, the more monodisperse the foam, the more the yield threshold Γ_0 increases. Indeed, polydispersity increases disorder in the flow and prevents the blockage of the constriction. However, the value of the threshold appears to vary only slightly with polydispersity: $\Gamma_0 = 1.7 \times 10^{-3}$ for $\delta = 15\%$ and $\Gamma_0 = 2.6 \times 10^{-3}$ for $\delta = 2.5\%$.

Beyond the threshold, two regimes are successively observed. In both of them, the flux of bubbles through the constriction increases in an affine manner with the pressure drop

$$Q = \begin{cases} 0 & \text{for} \quad \Gamma < \Gamma_0 \, , \\ \lambda_1 \left(\Gamma - \Gamma_0 \right) & \text{for} \quad \Gamma_0 < \Gamma < \Gamma_c \, , \\ \lambda_2 \left(\Gamma - \Gamma_c \right) + \lambda_1 \left(\Gamma_c - \Gamma_0 \right) & \text{for} \quad \Gamma > \Gamma_c \, . \end{cases} \tag{13}$$

In the first regime, the best affine fits of numerical points give

$$\begin{cases} \delta = 15\% : & \lambda_1 = 6.83 \pm 0.16, \\ \delta = 2.5\% : & \lambda_1 = 6.77 \pm 0.29. \end{cases} \tag{14}$$

Beyond a given value of the pressure gradient, the slope of the curve appears to decay suddenly: In this second regime, one obtains

$$\begin{cases} \delta = 15\% : & \lambda_2 = 1.32 \pm 0.08, \\ \delta = 2.5\% : & \lambda_2 = 1.18 \pm 0.09. \end{cases} \tag{15}$$

The transition between the two affine regimes happens at $\Gamma_c = 7.1 \times 10^{-3}$ for $\delta = 15\%$ and $\Gamma_c = 6.4 \times 10^{-3}$ for $\delta = 2.5\%$. Considering the uncertainty in the position of the transition, we cannot conclude that polydispersity has any influence on the value of Γ_c. First of all, let us remark that the decrease of the slope λ is rather counterintuitive, given that the same implementation of the bubble model predicts a shear-thinning behavior in a simple shear flow [Langlois *et al.* (2008)]. We would, therefore, rather expect the hydraulic resistance to decrease at high speeds: This tendency was observed by Bertho *et al.* (2006) in the "bubble silo," where the flowrate increases with effective gravity as a power law of index 3/2. However, it has been reported by Sexton *et al.* (2011) that at high shear rates bubbles tend to gather in lanes even in a polydisperse foam. This would increase order in the foam and, therefore, could favor temporary blockage at the constriction, inducing an increase of the hydraulic resistance. It has to be noted, though, that we could not observe any major qualitative difference between the two regimes in the nature of the flow, the shape of the streamlines, or the various averaged local properties presented in Sec. IV. However, Sexton *et al.* (2011) linked the change of rheology at high strain rates to a transition in velocity fluctuations of bubbles. To test this hypothesis in the present case, we define at each timestep the local velocity fluctuations

$$\delta v_x(x, y, t) = v_x(x, y, t) - \overline{v_x}(x, y) \quad \text{and} \quad \delta v_y(x, y, t) = v_y(x, y, t) - \overline{v_y}(x, y), \tag{16}$$

where the upper bar denotes a local average over the duration of the flow. The amplitude of these fluctuations is then averaged over the whole bulk of the channel and over time, and normalized by the average velocity at the entrance of the channel $v_0 = \tilde{Q}/W$

$$\frac{\Delta v_x}{v_0} = \frac{\langle |\delta v_x| \rangle}{v_0} \quad \text{and} \quad \frac{\Delta v_y}{v_0} = \frac{\langle |\delta v_y| \rangle}{v_0}. \tag{17}$$

Both quantities are plotted as a function of Γ in Fig. 5. At low speed, the velocity fluctuations are quite high (up to 70%), and both components decrease quickly when Γ is increased. However, with the change of regime at $\Gamma = \Gamma_c$ coincides a strong change of slope in the decay of velocity fluctuations, which then reach a quasisteady value: $36\% < \Delta v_x/v_0 < 39\%$ for $\Gamma > 0.007$.

Finally, we can remark that, especially in the slow regime (for low Γ), polydispersity does not have a major influence on the slope λ. Figure 6 shows that the flowrate increases monotonically with the width of the size distribution, all other control parameters being unchanged. This can be easily understood from the fact that polydispersity induces disordered motion by inhibiting the formation of lanes in a linearly sheared flow [Katgert *et al.* (2008); Sexton *et al.* (2011)]. Therefore, it makes the flow through the constriction more fluid, reducing the hydraulic resistance. The increase of Q with δ is more pronounced in the fast regime (for high Γ): Best affine fits give the relations

$$Q = \begin{cases} 0.014 + 0.040\,\delta & \text{for} \quad \Gamma = 4.6 \times 10^{-3} < \Gamma_c \\ 0.034 + 0.085\,\delta & \text{for} \quad \Gamma = 1.4 \times 10^{-2} > \Gamma_c. \end{cases} \tag{18}$$
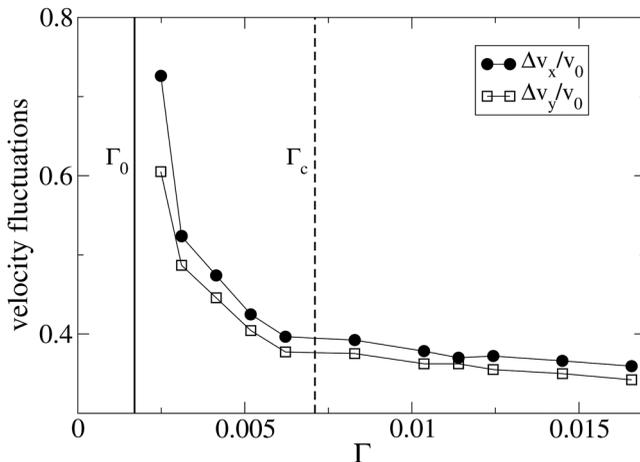
FIG. 5. Relative amplitude of velocity fluctuations as a function of the pressure drop.

This implies that for a given pressure drop and a given constriction width, the discharge can be increased by up to 50% simply by changing the polydispersity of the foam from 0% to 20%.

B. Width of the constriction

We varied the width of the constriction and measured the flowrate in the stationary regime for each case, for a polydisperse foam ($\delta = 15\%$; see Fig. 7). The foam flows only when the width of the hole exceeds a given threshold, the value of which decreases when the pressure drop increases. Beyond this threshold, the evolution of the flowrate with the width of the constriction can be fitted by a power law

$$
Q = \begin{cases} 0.034 \left(\dfrac{w}{R_0} - 2.8 \right)^{0.78} & \text{for} \quad \Gamma = 4.6 \times 10^{-3} \\[2ex] 0.135 \left(\dfrac{w}{R_0} - 1.5 \right)^{0.51} & \text{for} \quad \Gamma = 1.4 \times 10^{-2}. \end{cases} \tag{19}
$$

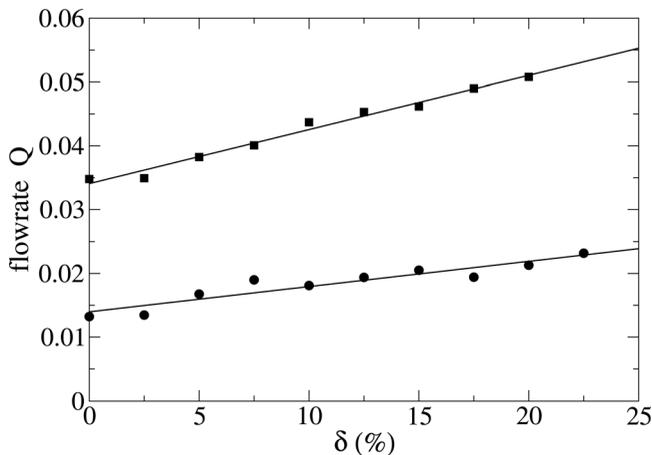**FIG. 6.** Flowrate as a function of polydispersity for $\Gamma = 4.6 \times 10^{-3} < \Gamma_c$ (●) and $\Gamma = 1.4 \times 10^{-2} > \Gamma_c$ (■). Plain lines are best affine fits of the data.
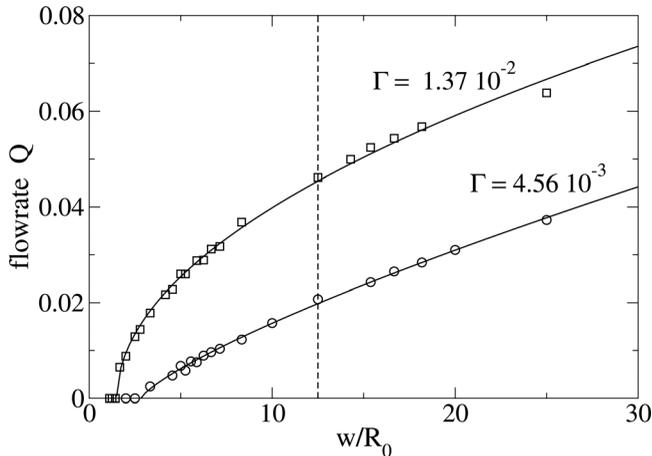
FIG. 7. Dimensionless flowrate of bubbles as a function of the width of the constriction for $\delta = 15\%$ and $\Gamma = 4.6 \times 10^{-3}$ (open circles) and $\Gamma = 1.4 \times 10^{-2}$ (open squares). Plain lines are best fits by power laws valid beyond the yield threshold [see Eq. (19)]. The dashed line corresponds to the default case $w/W = 4$.

The exponent of the power law is observed to decrease when the pressure drop is increased. Let us note that Bertho *et al.* (2006) also reported that the flowrate in the bubble silo increased like the square root of the width of the hole above a given threshold, which we observe here at high flowrate. It remains difficult, however, to assess a general law for the dependency of the flowrate Q in the three parameters δ, w/R_0, and Γ.

IV. LOCAL DESCRIPTION OF THE FLOW

In order to describe the local structure of the flow, we adopt the procedure described by Graner *et al.* (2008) and Marmottant *et al.* (2008). The mean scalar, vectorial, and tensorial quantities are calculated over a rectangular mesh in boxes whose size is comparable to the bubble area. These quantities are then averaged over at least 4000 images (representing 4×10^7 time-steps), after the steady state (characterized by the stability of the flowrate) has been reached. In all this section, we only represent the horizontal part of the channel.

A. Velocity field

The average velocity field in the slow regime for a polydisperse foam is presented in Fig. 8. The same plots in the fast regime show no apparent qualitative difference. The flow appears to be close to a plug flow both before and after the constriction. However, contrary to the experiments [Dollet (2010)] (see their Fig. 2), we do not observe any clear
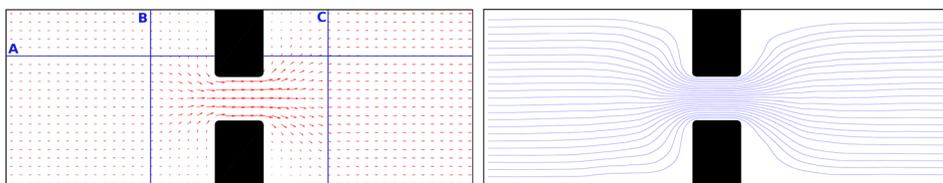

FIG. 8. Velocity field (left) and streamlines (right) for polydispersity $\delta = 15\%$ and pressure drop $\Gamma = 4.6 \times 10^{-3} < \Gamma_c$. Blue straight lines are transects A, B, and C used to plot velocity profiles in Fig. 9.
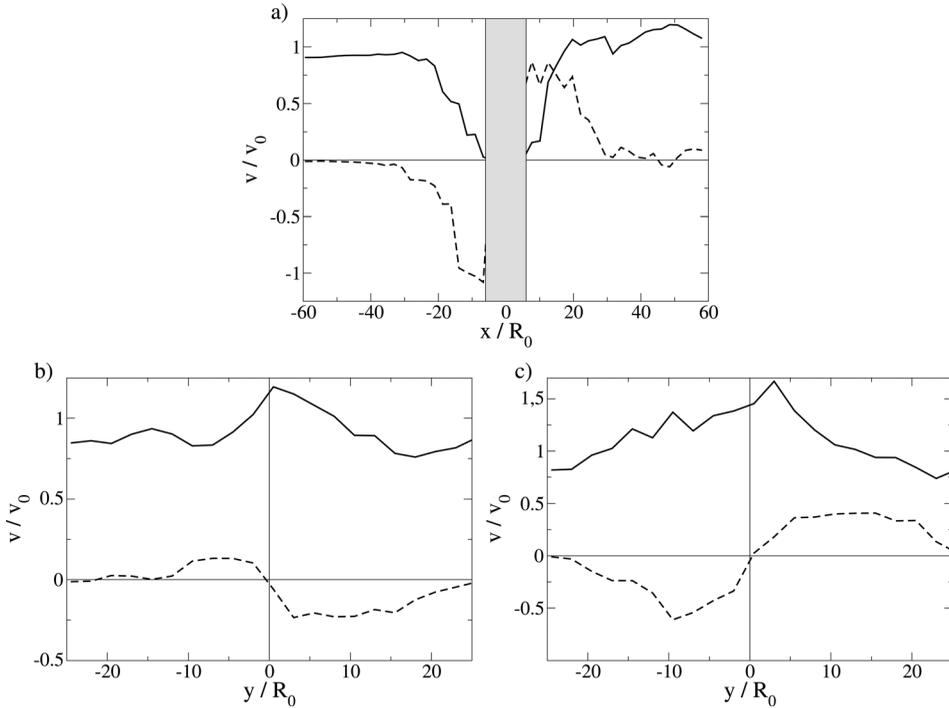
FIG. 9. Velocity components v_x (plain curves) and v_y (dashed curves) along (a) line A, (b) line B (upstream), and (c) line C (downstream). Velocity is normalized by the average velocity $v_0 = \bar{Q}/W$ at the entrance of the channel. Polydispersity is $\delta = 15\%$ and pressure drop $\Gamma = 4.6 \times 10^{-3} < \Gamma_c$.

refocusing of the streamlines after the obstacle. It is indeed understandable that the bubble model is less suited to describe a foam experiencing expansion, considering that bubbles only interact through compressive forces.

Velocity profiles are plotted in Fig. 9 along longitudinal transect A ($y = 11.9\ R_0$) and transverse transects B (upstream, $x = -22.8\ R_0$) and C (downstream, $x = 22.8\ R_0$). The velocity is normalized by its average value v_0. As can be seen in Figs. 9(a) and 9(b), the flow is almost a perfect plug flow at the entrance of the channel. After the constriction [see Fig. 9(c)], the x-velocity is slightly higher in the center of the channel than on the sides, which is due to the slow divergence of streamlines (which is also evidenced from the sign of v_y). As has been observed in experiments [Dollet (2010)], there is no deadzone nor vortices in the corners of the obstacle (neither upstream nor downstream). In Fig. 10(a), we plot the velocity profile along the central line of the channel, normalized by the maximal velocity reached in the constriction. We observe that the curves collapse relatively well on a single master curve, except when the pressure drop is very close to the yield threshold. The effective liquid fraction (that is, here, inversely correlated to the pressure on bubbles) can increase significantly between before and after the constriction, which explains why the velocity is systematically larger at the exit of the channel than at the entrance: The density of bubbles being lower than at the entrance, the flowrate is conserved. Finally, we can also note the presence of a small undershoot in velocity downstream of the constriction but only for very low velocities. This undershoot has also been observed experimentally by Dollet (2010) in a quasistatic flow and by Jones and Cox (2012) with simulations based on Surface Evolver. In Fig. 10(b), we compare the velocity profile obtained by Jones and Cox (2012) to the profile we obtain with the two extreme
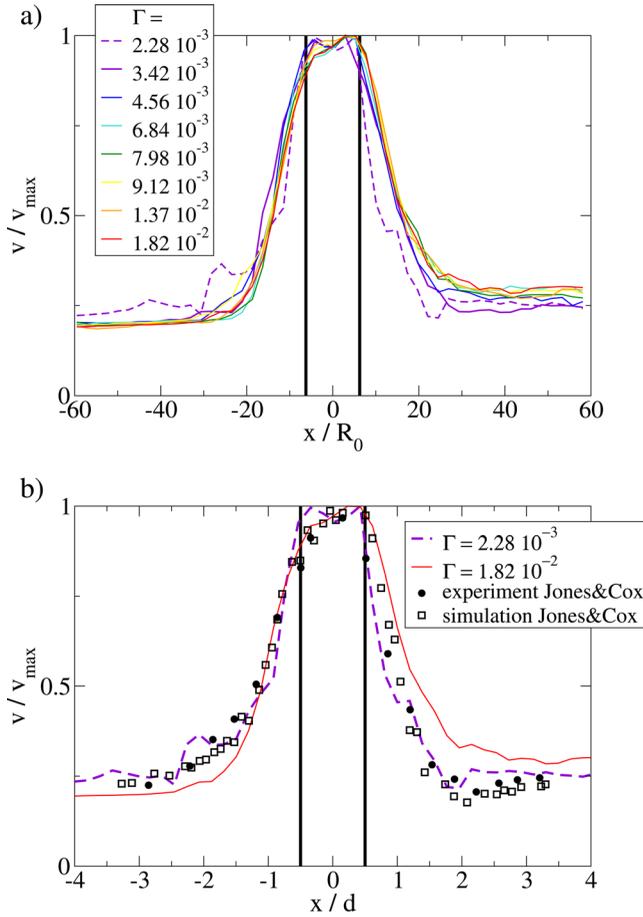
FIG. 10. (a) Normalized streamwise velocity profile along the central line ($y = 0$) for different values of the pressure drop Γ and polydispersity $\delta = 15\%$. (b) Our velocity profile in the slowest and fastest regimes is compared to experiments (disks) and Surface Evolver simulations (squares) by Jones and Cox (2012).

values of the pressure drop. The velocity is normalized by its maximal value and the x-coordinate by the length of the constriction. We can observe that the agreement between the bubble model and the quasistatic model is relatively good, especially in the case of a very slow motion, as can be expected.

B. Plasticity

The plasticity of the foam is measured by the density of T1 events that happen when two pairs of bubbles switch their neighbors. We define pairs of neighboring bubbles by computing the Delaunay triangulation of the bubble centers: Two bubbles are considered to be neighbors if their Voronoi domains share a common side. We then measure separately the local number of appearing (N_a) and disappearing (N_d) contacts in each box of area A_{box} and during a time T. The local frequency of T1s is then normalized by the surface of a bubble and the internal timescale

$$f_{T_1} = \frac{\pi R_0^2}{A_{box}} \frac{\tau}{T} \frac{N_a + N_d}{2}. \tag{20}$$
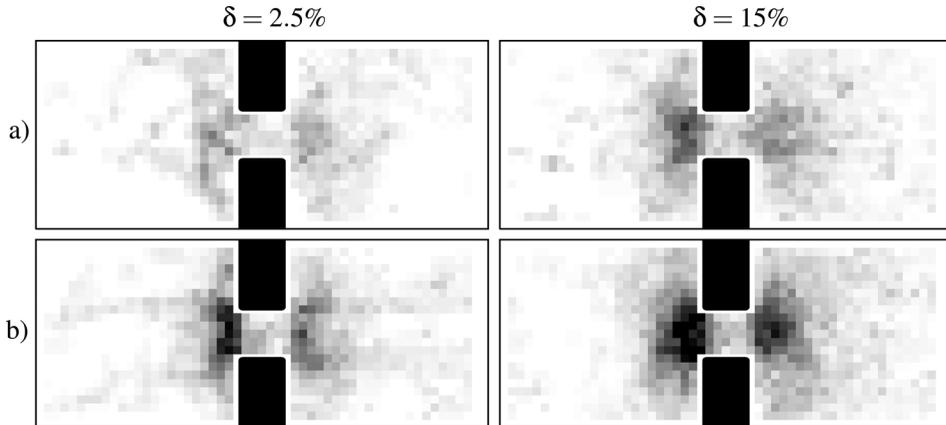
FIG. 11. Local frequency of T1s for both monodisperse and polydisperse samples and (a) $\Gamma = 3.4 \times 10^{-3}$ and (b) $\Gamma = 1.1 \times 10^{-2}$. Grayscale is arbitrary and identical for all figures.

The frequency of T1s is mapped for different values of the polydispersity and pressure drop in Fig. 11. We observe that the frequency of plastic events is always high close to the obstacle (both upstream and downstream) and lower inside the constriction itself. It increases slightly with polydispersity of the foam (that favors disorder) and more significantly with the flowrate. In all cases, there is a strong asymmetry between upstream and downstream, as can be easily seen in the profiles plotted in Fig. 12(a). In this figure, T1 frequencies obtained by Dollet (2010) and Jones and Cox (2012) are normalized by the maximal value obtained just before the constriction, to eliminate the influence of the flowrate. In all cases, the number of plastic events is higher just before the constriction than just after. One must note, however, that the position of the secondary peak of plasticity is systematically obtained closer to the constriction, and the asymmetry is less pronounced with the bubble model than in experiments and quasistatic simulations. We can also confirm that increasing the polydispersity of the foam enhances plasticity in the flow by facilitating T1 events and, therefore, reduces the hydraulic resistance. Figure 12(b) shows that the total number of T1s, averaged over the whole channel, increases affinely with the flowrate of bubbles, which is consistent with the fact that plastic events are triggered by local strain.

The plastic tensor **P**, as defined by Graner *et al*. (2008), gives information both about the frequency and the privileged direction of T1 events. The eigenvector corresponding to the positive eigenvalue of this tensor, which gives the preferential direction of bubble separation, is mapped in Fig. 13. Separation of bubbles appears to happen preferentially in the streamwise direction before the constriction, and in the transverse direction after the constriction.

C. Elastic strain

We compute the texture tensor **M** following the definition by Asipauskas *et al*. (2003) and Graner *et al*. (2008). This tensor describes quantitatively the pattern formed by bubbles: If a link between two neighboring bubbles is the vector $\ell = \begin{pmatrix} x \\ y \end{pmatrix}$, the texture tensor is defined by

$$\mathbf{M} = \langle \ell \otimes \ell \rangle = \begin{pmatrix} \langle x^2 \rangle & \langle xy \rangle \\ \langle xy \rangle & \langle y^2 \rangle \end{pmatrix}, \tag{21}$$
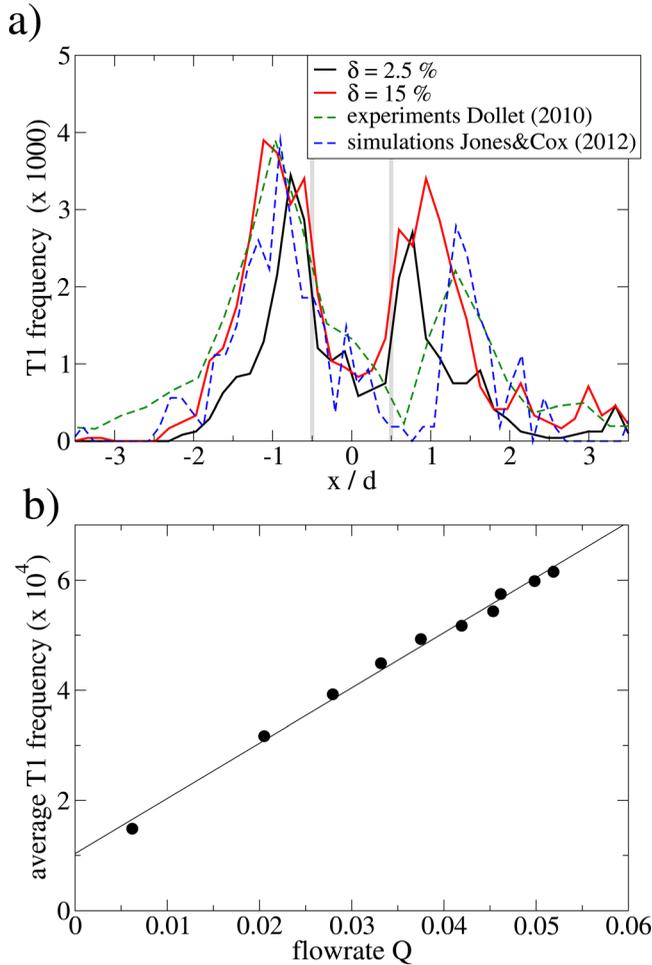
FIG. 12. (a) Number of T1s per unit bubble and internal timescale along the central line $y = 0$, for $\Gamma = 1.1 \times 10^{-2} > \Gamma_c$, compared with experimental data from Dollet (2010) and numerical data from Jones and Cox (2012) (personal communication). (b) Average T1 frequency in the channel as a function of the flowrate for $\delta = 15\%$ and same pressure drop.

where averaging is done over all links found in a given box and during a given time. The average square distance between neighbors is directly given by the trace of this tensor. The main direction of strain is given by the eigenvector associated with the largest eigenvalue [see Fig. 14(b)]. For a monodisperse 2D foam arranged in a hexagonal packing, the texture tensor would have two identical eigenvalues [see Fig. 14(a)].

Contrary to what happens in experiments and Surface Evolver or Potts model simulations [Jones *et al.* (2011)], bubbles in our model remain as disks and, therefore, cannot be much stretched nor compressed (small overlaps aside). This appears clearly if we compute the normalized extensional component of the texture tensor

$$M_n = \frac{M_{xx} - M_{yy}}{M_{xx} + M_{yy}} \,. \tag{22}$$

As can be seen in Fig. 15, in our simulations, $|M_n|$ does not exceed 0.1, whereas it can be of the order of 0.5 in experiments [Jones and Cox (2012)]. For more clarity, we plot the
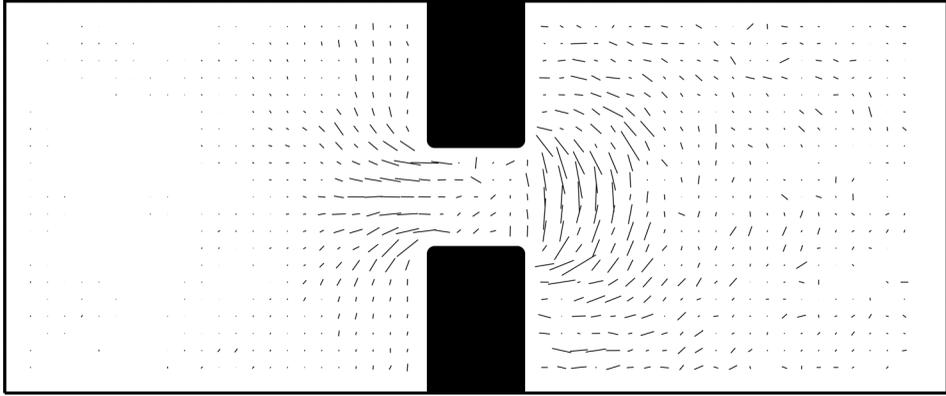
FIG. 13. Map of the plastic tensor for $\delta = 15\%$ and $\Gamma = 1.1 \times 10^{-2} > \Gamma_c$: Segments represent the direction associated with the positive eigenvalue of **P**, their length being proportional to the local T1 frequency.

same profile with an amplified value of M_n to make the comparison easier. As in experiments and quasistatic simulations, bubbles are extended streamwise before the constriction ($M_n > 0$) and transversally after the constriction ($M_n < 0$). However, one must note that in the bubble model, the sign inversion occurs in the middle of the constriction, whereas Jones and Cox (2012) find it just after the constriction. The absolute extension of bubbles in the bubble model is observed to be lower after the constriction than before, which is not the case in experiments. The very small values obtained for M_n imply that if we plot a map of the texture tensor, its representative ellipses look like circles, making it difficult to identify directions of compression and stretching. Therefore, we rather compute the deviatoric component of the texture tensor

$$\mathbf{M}_d = \mathbf{M} - \frac{\mathrm{Tr}(\mathbf{M})}{2}\,\mathbf{I}_2,\tag{23}$$

with $\mathbf{I}_2$ the identity matrix. The tensor $\mathbf{M}_d$ has two opposite eigenvalues: The eigenvector associated with the positive (respectively, negative) one gives the main direction of stretching (respectively, compression). We map the directions of stretching in Fig. 16:
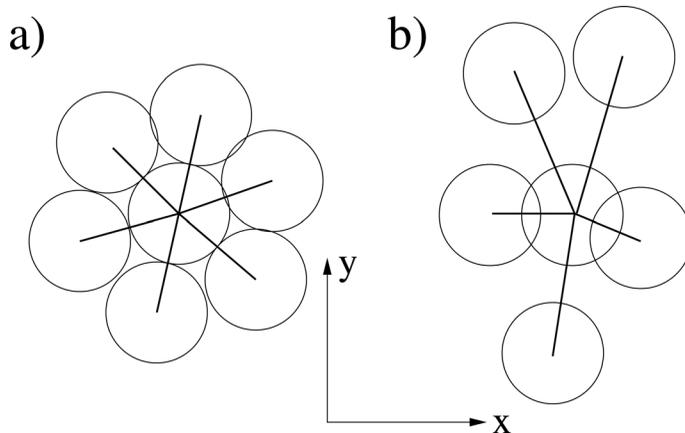

FIG. 14. Links between neighboring bubbles in two cases: (a) The texture tensor is diagonal and has two identical eigenvalues. (b) The eigenvectors of **M** are roughly aligned with axes x (eigenvalue λ_1) and y (eigenvalue $\lambda_2 > \lambda_1$).
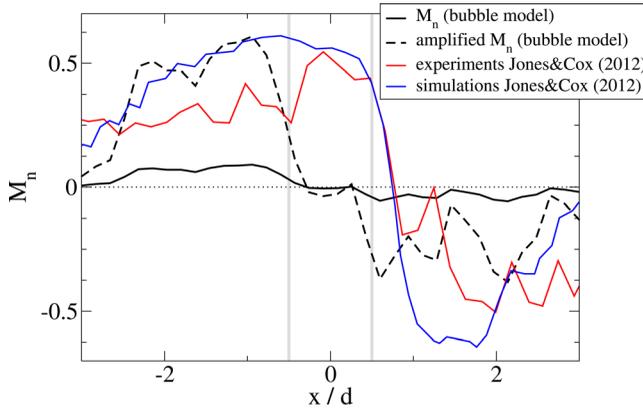
FIG. 15. Texture M_n along the central axis for $\delta = 15\%$ and $\Gamma = 1.1 \times 10^{-2}$. Experimental and numerical results by Jones and Cox (2012) are shown for comparison. To facilitate comparison, the dashed line represents the profile of M_n amplified so that it reaches the same maximum as in quasistatic simulations.

Bubbles appear to be stretched toward the constriction in the upstream part and spanwise in the downstream part. Let us note that the eigenvectors of the deviatoric texture $\mathbf{M}_d$ are identical to the eigenvectors of the internal strain $\mathbf{U}$, defined as the comparison between the observed texture and a texture of reference [Graner *et al.* (2008)].

D. Relation between strain and plasticity

The constitutive relation among the plastic, deformation, and strain tensors proposed by Marmottant *et al.* (2008) predicts that the plastic tensor and the elastic strain should be aligned. We check this prediction by choosing two regions of interest (red rectangles in Fig. 16), close to the constriction, where the amount of plastic events is significant. We compute at each point the angle $\theta(P, U)$ between the main direction of bubble separation (associated with the positive eigenvalue of $\mathbf{P}$) and the direction of stretching (associated with positive eigenvalue of $\mathbf{M}_d$). The distribution of these angles in each region of interest is plotted in Fig. 17. The average values of the angle are, respectively,
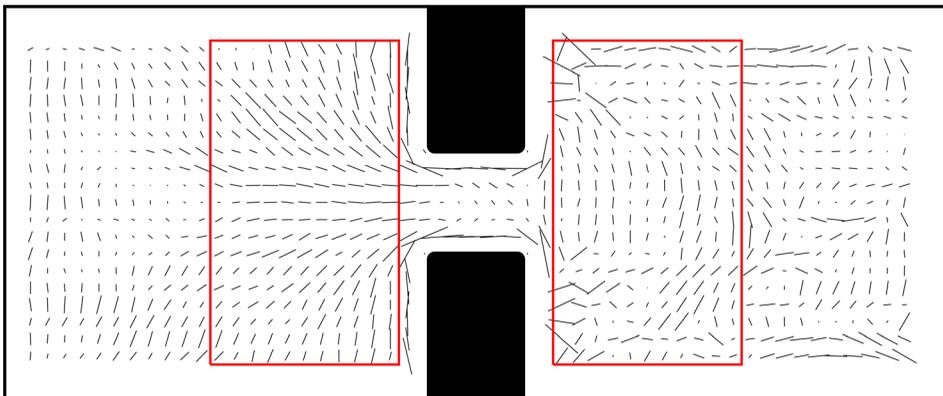

FIG. 16. Main directions of stretching for $\delta = 15\%$ and $\Gamma = 1.1 \times 10^{-2}$ (fast regime). Length of the segments is proportional to the corresponding eigenvalue of the deviatoric texture tensor. Red rectangles are the two regions of interest used in Sec. IV D.
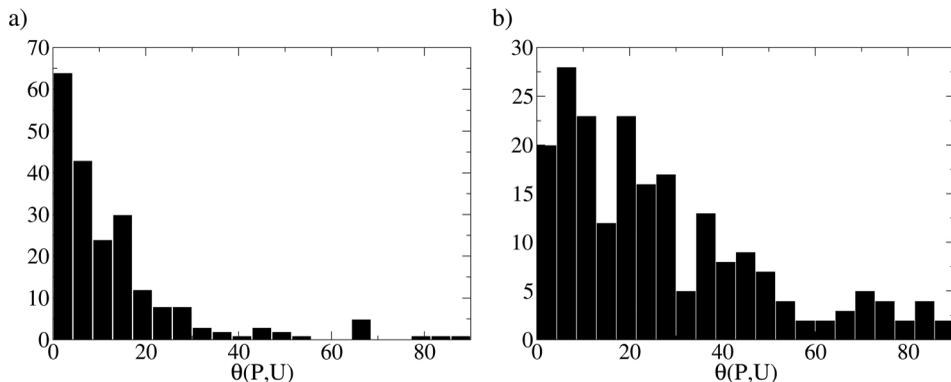
FIG. 17. Distribution of the angle between the major axes of the plastic and strain tensors in (a) the region upstream and (b) the region dowstream of the constriction. Polydispersity is $\delta = 15\%$ and pressure drop $\Gamma = 1.1 \times 10^{-2}$.

$$\begin{aligned}
\text{upstream:} &\quad \langle \theta(P,U) \rangle = 13.8°, \\
\text{downstream:} &\quad \langle \theta(P,U) \rangle = 26.9°.
\end{aligned} \tag{24}$$

As a comparison, in his experimental study, Dollet (2010) finds an average angle $\langle \theta(P,U) \rangle = 16°$ (although he uses the deviatoric stress tensor σ_d which is equivalent to U_d). We can conclude that the alignment between the major axes of tensors **P** and **U** is well verified in the region of high plasticity right before the constriction. After the obstacle, the major axes often diverge and this alignment is not verified anymore. However, it may seem natural since the bubble model is less suited to reproduce the dynamics of the foam after the constriction, where bubbles can be neighbors without physically interacting. This could explain why the agreement between the model and the theoretical prediction is better upstream than downstream. The good agreement in the upstream part of the flow tends to indicate that the compressive region (before the constriction) is well modeled and not affected by the fact that the flow downstream differs significantly from its experimental counterpart.

V. CONCLUSIONS

The bubble model, or soft-disk model, has been applied to the flow of a 2D foam through a constriction, and its predictions have been quantitatively compared with existing experimental [Dollet (2010); Jones and Cox (2012)] and numerical [Jones and Cox (2012)] results. This approach can be seen as complementary to quasistatic simulations based on Surface Evolver, since it applies to relatively wet foams and allows one to account for dynamic properties. Furthermore, it is simple to implement and requires only moderate computational times. The present study proves that its predictions are compatible with existing experimental observations in the constriction geometry.

We have shown that beyond a given threshold, the flowrate of bubbles increases affinely with the pressure drop applied to the foam. We also predict a further change of regime, with a sudden increase of the hydraulic resistance at high speeds, although this change of regime cannot be evidenced in the local properties of the flow. Beyond a minimal threshold, the flowrate of bubbles appears to grow like a power law of the width of the constriction, the index of which depends on the pressure drop. Finally, we predict that the width of the size distribution of bubbles has a critical influence on the flow: The frequency of plastic events and the flow velocity always increase with the polydispersity of

the foam. For a given pressure drop and a given constriction ratio, the flowrate can be increased by up to 50% simply by adding some polydispersity. These predictions could easily be verified in future experimental studies, although in most setups, the flowrate, and not the pressure drop, is imposed.

The bubble model also allows one to compute easily the local properties of the flow, such as the texture, strain, and plastic tensors. Because of the constraints of the model, the texture tensor is much more isotropic than in experiments or Potts and Surface Evolver simulations. However, the main axes of stretching agree with experimental observations, as does the spatial repartition of plastic events. In particular, we observe a strong density of T1s in the neighborhood of the constriction, with a clear asymmetry between upstream and downstream. Finally, although the bubble model appears less accurate downstream of the constriction, the alignment between plastic and strain tensors, predicted by a tensorial rheological model [Marmottant *et al.* (2008)], is well verified before the constriction.

Two major differences between the present simulations and experiments can be underlined: Bubbles are never stretched as much as they appear to be, close to the constriction, in experiments and Surface Evolver simulations, even if we take into account their Voronoi domains rather the spheres themselves. This could only be solved by computing the exact deformation of bubbles when in contact, which has been done for instance by Rognon and Gay (2008) but only for a small number of bubbles. Besides, the bubble model is more accurate upstream (where the foam experiences compression) than downstream (where it experiences expansion). This intrinsic limitation in the predictive ability of the bubble model is not due to the simplicity of the expression of local forces but due to the fact that bubbles only interact in compression, which is also the case in more realistic models such as the EHD model by Seth *et al.* (2011). This drawback could perhaps be solved, while keeping the simplicity of the bubble model, by adding tensile forces between neighboring bubbles, which would account for the presence of disjoining pressures in the foam.

ACKNOWLEDGMENTS

References

Asipauskas, M., M. Aubouy, J. A. Glazier, F. Graner, and Y. Jiang, "A texture tensor to quantify deformations: The example of two-dimensional flowing foams," Granular Matter **5**, 71–74 (2003).

Barry, J. D., D. Weaire, and S. Hutzler, "Nonlocal effects in the continuum theory of shear localisation in 2D foams," Philos. Mag. Lett. **91**(6), 432–440 (2011).

Bertho, Y., C. Becco, and N. Vandewalle, "Dense bubble flow in a silo: An unusual flow of a dispersed medium," Phys. Rev. E **73**, 056309 (2006).

Bocquet, L., A. Colin, and A. Ajdari, "Kinetic theory of plastic flow in soft glassy materials," Phys. Rev. Lett. **103**(3), 036001 (2009).

Bretherton, F. P., "The motion of long bubbles in tubes," J. Fluid Mech. **10**, 166–188 (1961).

Cheddadi, I., P. Saramito, B. Dollet, C. Raufaste, and F. Graner, "Understanding and predicting viscous, elastic, plastic flows," Eur. Phys. J. E **34**(1), 1–15 (2011).

Debrégeas, G., H. Tabuteau, and J.-M. di Meglio, "Deformation and flow of a two-dimensional foam under continuous shear," Phys. Rev. Lett. **87**, 178305 (2001).

Denkov, N. D., V. Subramanian, D. Gurovich, and A. Lips, "Wall slip and viscous dissipation in sheared foams: Effect of surface mobility," Colloids Surf., A **263**, 129–145 (2005).

Dollet, B., "Local description of the two-dimensional flow of foam through a contraction," J. Rheol. **54**, 741–760 (2010).

Dollet, B., and F. Graner, "Two-dimensional flow of foam around a circular obstacle: Local measurements of elasticity, plasticity and flow," J. Fluid Mech. **585**, 181–211 (2007).

Dollet, B., F. Elias, C. Quilliet, C. Raufaste, M. Aubouy, and F. Graner, "Two-dimensional flow of foam around an obstacle: Force measurements," Phys. Rev. E **71**(3), 031403 (2005b).

Dollet, B., M. Aubouy, and F. Graner, "Anti-inertial lift in foams: A signature of the elasticity of complex fluids," Phys. Rev. Lett. **95**, 168303 (2005a).

Durian, D. J., "Foam mechanics at the bubble scale," Phys. Rev. Lett. **75**, 4780–4783 (1995).

Durian, D. J., "Bubble-scale model of foam mechanics: Melting, nonlinear behavior, and avalanches," Phys. Rev. E **55**, 1739–1751 (1997).

Goyon, J., A. Colin, G. Ovarlez, A. Ajdari, and L. Bocquet, "Spatial cooperativity in soft glassy flows," Nature **454**(7200), 84–87 (2008).

Graner, F., B. Dollet, C. Raufaste, and P. Marmottant, "Discrete rearranging disordered patterns, Part I: Robust statistical tools in two or three dimensions," Eur. J. Phys. E **25**, 349–369 (2008).

Höhler, R., and S. Cohen-Addad, "Rheology of liquid foam," J. Phys.: Condens. Matter **17**, 1041–1069 (2005).

Janiaud, E., D. Weaire, and S. Hutzler, "Two-dimensional foam rheology with viscous drag," Phys. Rev. Lett. **93**, 18303 (2006).

Jiang, Y., P. J. Swart, A. Saxena, M. Asipauskas, and J. A. Glazier, "Hysteresis and avalanches in two-dimensional foam rheology simulations," Phys. Rev. E **59**, 5819–5832 (1999).

Jones, S. A., B. Dollet, N. Slosse, Y. Jiang, S. J. Cox, and F. Graner, "Two-dimensional constriction flows of foams," Colloids Surf., A **382**, 18–23 (2011).

Jones, S. A., and S. J. Cox, "On the effectiveness of a quasistatic bubble-scale simulation in predicting the constriction flow of a two-dimensional foam," J. Rheol. **56**, 457–471 (2012).

Katgert, G., and M. van Hecke, "Jamming and geometry of two-dimensional foams," Europhys. Lett. **92**(3), 34002 (2010).

Katgert, G., M. E. Möbius, and M. van Hecke, "Rate dependence and role of disorder in linearly sheared two-dimensional foams," Phys. Rev. Lett. **101**, 058301 (2008).

Langlois, V. J., S. Hutzler, and D. Weaire, "Rheological properties of the soft-disk model of two-dimensional foams," Phys. Rev. E **78**, 021401 (2008).

Lauridsen, J., G. Chanan, and M. Dennin, "Velocity profiles in slowly sheared bubble rafts," Phys. Rev. Lett. **93**, 018303 (2004).

Marmottant, P., C. Raufaste, and F. Graner, "Discrete rearranging disordered patterns, Part II: 2D plasticity, elasticity and flow of a foam," Eur. J. Phys. E **25**, 371–384 (2008).

Meeker, S. P., R. T. Bonnecaze, and M. Cloitre, "Slip and flow in soft particle pastes," Phys. Rev. Lett. **92**(19), 198302 (2004).

Pöschel, T., and T. Schwager, *Computational Granular Dynamics: Models and Algorithms* (Springer-Verlag, Berlin, 2005).

Rognon, P., and C. Gay, "Soft dynamics simulation. 1. Normal approach of two deformable particles in a viscous fluid and optimal-approach strategy," Eur. Phys. J. E **27**(3), 253–260 (2008).

Saramito, P., "A new elastoviscoplastic model based on the Herschel-Bulkley viscoplastic model," J. Non-Newtonian Fluid Mech. **158**, 154–161 (2009).

Saugey, A., W. Drenckhan, and D. Weaire, "Wall slip of bubbles in foams," Phys. Fluids **18**, 053101 (2006).

Seth, J. R., L. Mohan, C. Locatelli-Champagne, M. Cloitre, and R. T. Bonnecaze, "A micromechanical model to predict the flow of soft particle glasses," Nature Mater. **10**(11), 838–843 (2011).

Sexton, M. B., M. E. Möbius, and S. Hutzler, "Bubble dynamics and rheology in sheared two-dimensional foams," Soft Matter **7**(23), 11252–11258 (2011).

Tighe, B. P., E. Woldhuis, J. C. Remmers, W. van Saarloos, and M. van Hecke, "Model for the scaling of stresses and fluctuations in flows near jamming," Phys. Rev. Lett. **105**(8), 088303 (2010).

Weaire, D., and S. Hutzler, *The Physics of Foams* (Oxford University Press, Oxford, 1999).

Weaire, D., S. Hutzler, V. J. Langlois, and R. J. Clancy, "Velocity dependence of shear localisation in a 2D foam," Philos. Mag. Lett. **88**, 387–396 (2008).